



Modeling optical floating zone crystal growth in a high-pressure, single-lamp furnace

Scott S. Dossa^a, Jeffrey J. Derby^{b,*}

^a School of Physics and Astronomy, University of Minnesota, Tate Hall, 116 Church Street SE, Minneapolis, MN 55455, USA

^b Department of Chemical Engineering and Materials Science, University of Minnesota, 151 Amundson Hall, 421 Washington Avenue SE, Minneapolis, MN 55455, USA



ARTICLE INFO

Communicated by Chung wen Lan

Keywords:

- A1. Computer simulation
- A1. Convection
- A1. Fluid flows
- A1. Heat transfer
- A2. Floating zone technique
- B1. Oxides

ABSTRACT

An optical floating zone (OFZ) model is developed, validated, and applied to obtain initial results for crystal growth in a novel high-pressure, single-lamp furnace. Computation with a realistic irradiation profile for zone heating results in dramatically different growth behavior than predicted using idealized Gaussian heating, though the discontinuities of the realistic profile prove challenging from a computational perspective. System pressure significantly affects buoyant flows in the surrounding atmosphere. Both driving force and flow strength increase nonlinearly with pressure, with the Grashof number growing with the cube of pressure and the Reynolds number scaling with pressure to the 3/2 power. For pressures of 100 bar and greater, flows of the surrounding phase strongly cool the growth sample, leading to significantly shorter melt zones, more deflected melt-solid interfaces, and weaker flows in the melt zone. Such effects reduce the likelihood of achieving stable growth conditions under very high pressure in this OFZ system.

1. Introduction

The optical floating zone (OFZ) system is a workhorse in the search for new materials and is particularly well suited for the growth of oxide single crystals due to their high absorptivity in the infrared spectrum and their high melting temperatures [1]. The OFZ system, depicted in Fig. 1(a), is characterized by several features that make it very useful for growing small crystals, relatively quickly, of a wide range of materials. The energy of the heating lamp is readily focussed to a small region of space, providing the ability to heat to very high temperatures, well above the melting point of most compounds of interest. This melted, liquid “floating zone” is relatively small and contained by a meniscus that is supported against gravity by surface tension. Crystal growth occurs by the translation of a polycrystalline feed rod into the zone and simultaneous pulling of a crystal out of the zone.

Since the floating zone is bounded only by the feed rod, crystal, and liquid-gas interface, the high-temperature, molten liquid does not contact the inner walls of a containing ampoule. This eliminates contamination from the container and removes other, potentially deleterious interactions, such as stresses induced at the point of contact between the solid-liquid interface and the container wall. OFZ growth under high pressure in a transparent enclosure offers additional advantages [2–5],

such as the potential to suppress the evaporation of volatile components from the sample when an inert atmosphere is employed. In addition, a high-pressure atmosphere of an active component, such as oxygen, can be employed to change the chemical potential of the surrounding fluid phase and access a much richer phase space for the solidification of new materials [6–11].

However, successful growth in optical floating zone systems is sometimes challenging, which can significantly slow the process of materials discovery. In a recent overview, Dabkowska and Dabkowski [1] touted the many successes of this technique for the growth of new classes of oxide materials. However, they note that growth is frequently difficult and that success often relies on intuition built from prior experience of the practitioner. The utility of the OFZ for materials discovery was also emphasized by Mitchell [3], who described the use of high pressures to access the growth of novel materials, such as rare-earth nickelate crystals [12–14]. Mitchell emphasized that gaps in operational knowledge, particularly under high pressure conditions, have proven problematic and that more fundamental understanding of crystal growth behavior is needed to truly take advantage of the optical floating zone system. Finally, Phelan et al. [5] explain how high-pressure floating zone systems are expanding the frontier in new materials synthesis and discovery but also show examples of how poor zone shape, concave

* Corresponding author.

E-mail address: derby@umn.edu (J.J. Derby).

melting interfaces, and flow instabilities have all hampered growth.

Concerning these challenges, Dabkowska and Dabkowski [1] asserted that "It would be very beneficial for scientific development of the OFZ methods if more modeling for different oxides is performed. Then it will be possible to connect growth features with the applied change of growth conditions." This provides the motivation for the work presented here, where we develop computational models to faithfully represent high-pressure optical floating zone crystal growth systems. In particular, we develop and present initial results representing the unique features of the high-pressure, single-lamp HKZ (Hochdruck-Kristallzüchtungsanlage) OFZ furnace developed by SciDre (Scientific Instruments Dresden) [15], which is the system employed in the aforementioned materials discovery efforts [3–14].

There has been substantial prior work on modeling floating zone crystal growth, including notable initial work by Durandau and Brown [16] and extensive analyses of optical floating zone systems by Lan and co-workers [17–31]. Durandau and Brown [16] were the first to rigorously account for the unknown positions of meniscus and melt-solid interfaces that describe the melt-zone shape in a conduction-dominated, two-dimensional (2D), axisymmetric model. To specify incoming thermal energy, they prescribed a far-field temperature rather than accounting for the distribution of light from a lamp source. A later study by Lan and Kou [19] was the first fully self-consistent model to include both conduction and convection, including buoyant and Marangoni flows in the liquid zone. The first model to account for the incoming distribution of light from a heating lamp was presented later by Lan and Tsai [27]; however, fluid flow in the zone was not considered in this model. Ratnicks et al. [32] presented a comprehensive model for an electromagnetically heated, industrial-scale floating zone system for silicon crystal growth that extended the prior effort of Mühlbauer et al. [33] to rigorously represent free boundaries and detailed system heat transfer.

Few prior models for the floating zone process have computed flows within the surrounding gas phase. Sabanski et al. [34] presented three

dimensional (3D) numerical simulations of the gas-phase flow, melt flow and dopant transport in both phases for float zone silicon growth; however, they ignore heat transfer in the gas phase and employ a fixed geometry determined by a simpler 2D calculations. Han et al. [35,36] considered gas-phase flow and its effect on growth in 3D models with a mixture of free and fixed interfaces. Recently, Fan and Liang [37] compute the effects of gas flows on the meniscus of a liquid bridge anchored between two rods as a model for studying floating zones.

Here, we develop and validate a base thermal-capillary model for the optical floating zone crystal growth system, including the representation of heat transfer, free boundaries that define the floating zone, and fluid flows within the liquid zone. We address significant new challenges needed to extend this approach to model the HKZ furnace, specifically the irradiation profile incident on the crystal and fluid flow and heat transfer within the surrounding atmosphere. The single-lamp, two-mirror configuration of this system has not been represented in prior floating zone models nor has any prior model included a detailed accounting of buoyant flows of the surrounding volume of gas or fluid, especially under high pressures. Finally, we present initial results that demonstrate the importance of these phenomena during optical floating zone crystal growth in the HKZ system.

2. Thermal-capillary base model

Our thermal-capillary base model for the OFZ system represents phenomena associated with zone formation, melting, and growth over the domains indicated in Fig. 1(b). A sample finite-element mesh used for numerical solution of the governing equations is also shown in the figure. In this model, we apply simple approximations for zone heating and do not explicitly consider flows in the gas/fluid atmosphere surrounding the sample, effects that will be discussed in subsequent sections.

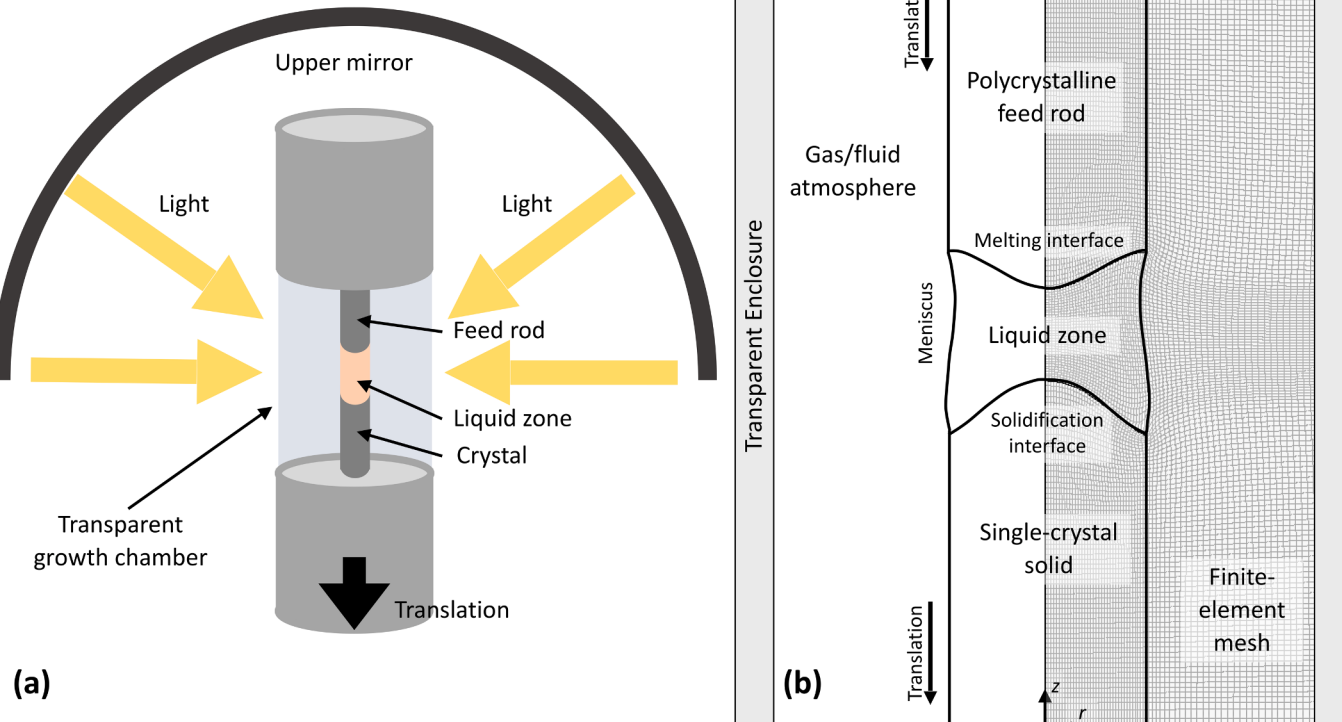


Fig. 1. (a) The HKZ optical floating zone furnace consists of a transparent enclosure containing the sample that is translated past the focal point of light reflected from the upper mirror. The focused light locally melts the sample to form a liquid zone, from which a single crystal may be grown under suitable conditions. (b) Model schematic including finite-element mesh.

2.1. Governing equations

Our base model for the OFZ closely follows the formulations first put forth by Duranceau and Brown [16] and Lan and Kou [19]. We assume that behavior is dominated by two-dimensional, axisymmetric phenomena and that the growth system is operating under quasi-steady conditions, whereby the melting and growth interfaces are presumed to advance at the applied translation rate and the effects of the changing length of feed rod and crystal are negligible. All equations are presented in the laboratory frame, wherein the liquid-melt interfaces are stationary and the feed and crystal translate downwards with a constant velocity, \mathbf{u}_s . Regarding notation, scalars (ρ) will be unbolded, vectors (\mathbf{u}) will be bolded and lower-case, and tensors (\mathbf{T}) will be bolded and upper-case.

2.1.1. Temperature fields

The steady-state temperature field over all domains is calculated using the following equation for energy conservation,

$$\mathbf{u} \cdot \nabla T = \frac{k_i}{\rho_i C_{p,i}} \nabla^2 T. \quad (1)$$

Here, i denotes the material associated with each domain (indices s, ℓ , and g in subsequent equations refer to solid, liquid, and gas), \mathbf{u} is the velocity within the medium, which corresponds to fluid motion within the liquid zones and solid-body translation for the feed rod and crystal. The temperature is denoted by T , k_i is the thermal conductivity, ρ_i is the density, and $C_{p,i}$ is the heat capacity. Spatial derivatives are represented in the 2D, cylindrical coordinate system by gradient operator $\nabla \equiv \partial/\partial \mathbf{e}_r + \partial/\partial \mathbf{e}_z$, where \mathbf{e}_r and \mathbf{e}_z are unit coordinate vectors, whose origin is placed along the centerline at the bottom surface of the crystal domain. The temperature field is continuous between all domains, and additional boundary conditions needed to make the problem well-posed are discussed below.

Along the solid-liquid interfaces for melting and solidification, heat fluxes are balanced via,

$$k_\ell \mathbf{n} \cdot \nabla T|_\ell - k_s \mathbf{n} \cdot \nabla T|_s = \rho_i \Delta H \mathbf{n} \cdot \mathbf{u}_s. \quad (2)$$

Here ΔH is the latent heat of fusion, \mathbf{u}_s is the translation rate of feed and crystal, and \mathbf{n} is a unit vector normal to the interface, directed from solid to liquid.

Along the outer surface of the sample, we consider heat transfer to a Gaussian far-field temperature profile to represent the effects of optical heating, identical to the approach employed in earlier models [16,19],

$$-k_i \mathbf{n} \cdot \nabla T|_i = h(T - T_\infty(z)) + \sigma_B \varepsilon_i (T^4 - T_\infty^4(z)), \quad (3)$$

where \mathbf{n} is a unit vector normal to the surface pointing outward, h is a Newtonian heat transfer coefficient to account for convective cooling of the surface, σ_B is the Stefan-Boltzmann constant, ε_i is the surface emissivity, and the Gaussian far-field temperature profile is given by,

$$T_\infty(z) = (T_{\max} - T_0) e^{\left(\frac{z-z_0}{\sigma_G}\right)^2} + T_0. \quad (4)$$

Here, the parameters describing the heat profile are: T_{\max} the maximum temperature, T_0 the background temperature level, σ_G the profile width, and z_0 the center of the applied temperature distribution in the axial direction. We emphasize that this simple representation of system heating is only used to validate our base thermal-capillary model against prior results in Section 2.3 and that our analyses of growth states in the high-pressure HKZ furnace employ the more rigorous representation of optical irradiation described in Section 3.

Finally, axisymmetry dictates a centerline boundary condition of

$$\mathbf{e}_r \cdot \nabla T = 0, \quad (5)$$

and far-field conditions of

$$\mathbf{e}_z \cdot \nabla T = 0, \quad (6)$$

are applied to the upper surface of the feed rod and the lower surface of the crystal.

2.1.2. Flow fields

Steady-state flows in fluid domains are calculated via the Navier-Stokes equations written for an incompressible fluid with the Boussinesq approximation to account for thermally-driven buoyant forces,

$$\rho_i \mathbf{u} \cdot \nabla \mathbf{u} = \nabla \cdot \mathbf{T} + \rho_i \mathbf{g} (1 - \beta_i (T - T_0)), \quad (7)$$

$$\nabla \cdot \mathbf{u} = 0, \quad (8)$$

where \mathbf{T} is the stress tensor, defined as,

$$\mathbf{T} = -p \mathbf{I} + \mu_i (\nabla \mathbf{u} + (\nabla \mathbf{u})^T). \quad (9)$$

Here, \mathbf{u} is the fluid velocity, \mathbf{g} is gravitational acceleration vector, β_i is the thermal expansion coefficient, T_0 is a reference temperature, p is the pressure field, μ_i is the fluid viscosity, and the superscript T denotes transpose.

Boundary conditions applied to the solid-liquid interfaces enforce local mass conservation and no-slip for the normal and tangential components of the flow, respectively,

$$\mathbf{n} \cdot (\rho_s \mathbf{u}_s - \rho_\ell \mathbf{u}_\ell) = 0, \quad (10)$$

$$\mathbf{t} \cdot (\mathbf{u}_s - \mathbf{u}_\ell) = 0. \quad (11)$$

Here \mathbf{u}_ℓ is the fluid velocity evaluated at the solid-liquid interfaces, \mathbf{u}_s is the translation rate of the solid feed rod and crystal, and \mathbf{t} denotes a unit vector that is tangent to the interface.

For boundary conditions along the melt meniscus, we apply a force balance that accounts for surface tension in the direction normal to the interface and Marangoni forces in the tangential direction. These two conditions are written in a single vector equation as,

$$\mathbf{n} \cdot \mathbf{T}|_\ell = 2\mathcal{H} \sigma \mathbf{n} + \nabla_s \sigma. \quad (12)$$

Here, \mathbf{n} is an outward-pointing unit vector normal to the meniscus, \mathcal{H} is the mean surface curvature, σ is surface tension, and ∇_s is the surface gradient operator.

Finally, we impose appropriate symmetry conditions of no tangential stress and no normal flow along the centerline of the liquid zone,

$$\mathbf{e}_z \cdot (\mathbf{e}_r \cdot \mathbf{T}|_\ell) = 0, \quad (13)$$

$$\mathbf{e}_r \cdot \mathbf{u}_\ell = 0. \quad (14)$$

2.1.3. Free boundaries

The most challenging aspect of problem formulation is the self-consistent representation of the four free boundaries that determine the geometry of a quasi-steady state of the floating zone system. We follow the approach of Duranceau and Brown [16], who first sorted the relationships defining the crystal radius, the melting and growth interfaces, and the zone meniscus.

First, we assume the feed and crystal rods are of equal density and are therefore translated at the same rate in a steady-state model. Assumption of quasi-steady behavior then dictates that the free boundary associated with the radius of the growing crystal is the same as that of the pull rod.

Determination of the locations of the three other free boundaries is more challenging. The locations of the two solid-liquid interfaces are determined by matching the local temperature to the melting temperature (T_m) of the material, yielding the classical isotherm condition [38–40] along each interface,

$$T = T_m.$$
(15)

Note that these conditions presume that the kinetics of melting and solidification are much faster than heat transfer and that both interfaces are isotropic and atomically rough [41].

The meniscus containing the liquid zone must connect to the edges of the melting and freezing interfaces, which also satisfies two degrees of freedom associated with the second derivatives of surface shape that are contained in the mean curvature term of Eq. (12). The shape of the meniscus is then determined via a kinematic condition that specifies that no liquid crosses the liquid-gas interface, which is represented as,

$$\mathbf{n} \cdot (\mathbf{u}_l - \mathbf{u}_g) = 0. \quad (16)$$

Note that our base thermal-capillary model assumes that the gas phase velocity, \mathbf{u}_g , is zero at the interface; we describe the consideration of gas phase flows in Section 4.

Finally, the Navier-Stokes equations specify the pressure field in any enclosed liquid domain up to an arbitrary constant, which we refer to as the pressure datum. As first elucidated by Duranteau and Brown [16], this constant appears directly within the liquid zone stress tensor and thus also in the normal component of the force balance along the meniscus; see Eqs. (9) and (12). Following [16], we solve for this pressure datum to alter the shape of the melt meniscus so that a growth angle condition is enforced via the implicit condition,

$$\mathbf{n} \cdot \mathbf{e}_r = \cos(\theta_g). \quad (17)$$

Here, θ_g is the angle formed between the liquid-gas meniscus and the solid-liquid growth interface. This growth angle is posited to be a constant determined by the equilibrium energies of the interfaces connecting at the tri-junction of the crystal, melt, and gas phases [42–45].

2.2. Numerical solution

The governing equations are solved numerically via the Galerkin Finite Element Method [46–50]. The temperature and velocity fields are approximated using continuous, biquadratic polynomial basis functions defined over each quadrilateral element. Pressure is approximated using lower-order continuous, bilinear basis functions. The finite element mesh is defined so that the positions of the free boundaries lie along selected element edges, making the mesh itself part of the solution to the problem. Interior mesh motion is determined via an Arbitrary Lagrangian-Eulerian approach, as described by Sackinger et al. [51], that treats the mesh as a pseudo-elastic solid with local displacements represented using the same biquadratic polynomials as used for the temperature and velocity fields.

All discretized equations are simultaneously solved using a Newton-Raphson method that employs the SuperLU matrix solver [52] for direct solution of the linearized residual equations. Our code is built upon Goma 6.0, an open-source program uniquely designed to handle multiphysics problems of heat, fluid, and species transport with free and moving boundaries at the continuum scale [53].

A finite-element mesh for a converged solution, depicted in Fig. 1(b), shows how the mesh deforms to follow the shapes of the free boundaries. Meshes were tested to assure convergence and accuracy of computed solutions. A typical mesh for the base model calculations employed 5,600 elements and a total of 83,086 unknowns, while a typical mesh for the high-pressure gas-phase model, described in Section 4, used 16,400 elements with 305,875 unknowns. When performed on a single-core of an Intel Xeon Gold 6230 processor, a single Newton iteration of the full system required 14.6 s for the base model and 120.9 s for the high-pressure gas-phase model.

The coupling of the free boundaries with all other fields makes this problem extremely nonlinear. With very good initial guesses, converged solution are found within 5–6 Newton iterations. However, a judicious computational strategy is needed to find initial solutions, and

continuation methods [54] prove to be invaluable for obtaining new solutions under changing parameters.

2.3. Base model validation

Our thermal-capillary base model is validated against the results of Lan and Kou [19], who computed axisymmetric, quasi-steady solutions for the growth of NaNO₃ in a floating zone system. Lan and Kou [19] employed a far-field Gaussian heating profile, identical to that described by Eq. (3), and considered a 0.4 cm-diameter crystal grown at 0.5256 cm/hr. We note that Lan and Kou employed control-volume discretization rather than the Galerkin finite-element approach of our model.

We should note that the temperature contour spacing in Fig. 2 is twice as wide in the solid as in the liquid. This was done to be consistent with Lan's image.

The solutions obtained from the two different models are directly compared in Fig. 2. First, we note that the shapes of the meniscus and solid-liquid interfaces are nearly identical between the two models. Focusing in on solution details, the flows in the liquid zone, shown on the left of each plot by streamfunction contours with constant spacing, agree well in form and strength, with two vortices that are driven primarily by Marangoni stresses along the melt meniscus. The upper flow vortex rotates in the clockwise direction, while the lower vortex is slightly stronger and flows counter-clockwise.

Temperature fields are shown on the right of each plot, where five evenly spaced isotherms are plotted in the melt for each simulation and the same spacing for isotherms is used for the solid regions. The temperature contours for both model results are nearly identical shape. Finally, the maximum temperature predicted by our thermal-capillary base model is 317.81 °C and located near the mid-point of the meniscus; this corresponds almost exactly to the maximum temperature of 317.62 °C predicted by the model of Lan and Kou.

3. Irradiation model

There have been few prior optical floating zone models that have gone beyond the simple representation of heating by a Gaussian profile. As mentioned in the introduction, Lan and Tsai [27] were the first to analyze the details of irradiation and heat transfer in the optical floating zone. In particular, they realized that amount of energy absorbed is affected by the relative angle between the incoming light and the normal to the melt meniscus. This additional coupling of optical energy distribution and absorption to an already highly non-linear problem has proven a challenge for modeling. Later analyses of Rivas et al. [55–59] considered the irradiation of cylindrical samples in side-lit, ellipsoidal-mirror optical furnaces. These analyses computed temperature fields that arose from such heating but did not consider the free boundaries of the floating zone crystal growth system.

More recently, Souptel, Löser, Behr, and co-workers [60,61] derived irradiation profiles for the single-lamp, two-mirror ScIDre HKZ furnace [15] depicted schematically in Fig. 3(a). This system employs a single heating lamp whose power is redirected by two vertically oriented, ellipsoidal mirrors. The vertical orientation has a distinct advantage in that the heating is significantly more axisymmetric than in other designs that employ side-mounted heating lamps. However, this vertical configuration results in asymmetries in axial energy deposition that affect growth behavior. Below, we extend the analyses by Souptel et al. [60,61] to formulate an irradiation profile from geometric and optical principles and then apply the associated optical energy distribution to more rigorously represent zone heating in our thermal-capillary model.

3.1. Governing equations

We aim to extend our prior, idealized heat flux boundary condition that utilized a Gaussian heating profile, Eq. (3), with energy input according to the incident light profile from the lamp as,

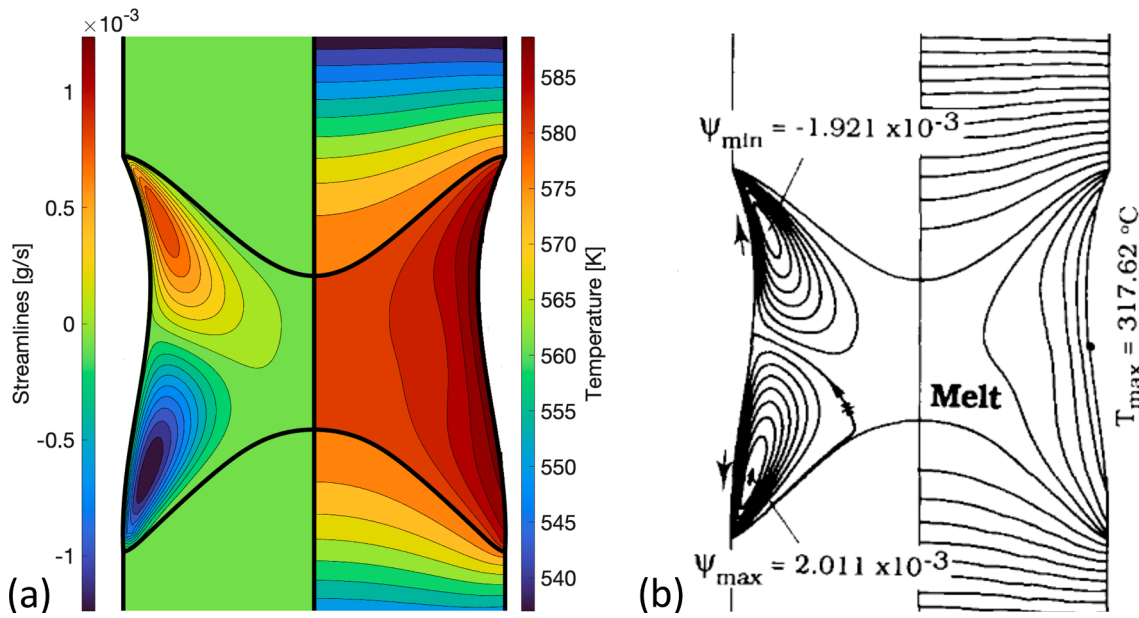


Fig. 2. Model results for the floating zone growth of NaNO_3 under a Gaussian heating profile are shown for (a) the thermal-capillary base model developed here and (b) the prior model of Lan and Kou [19] (figure reproduced with permission).

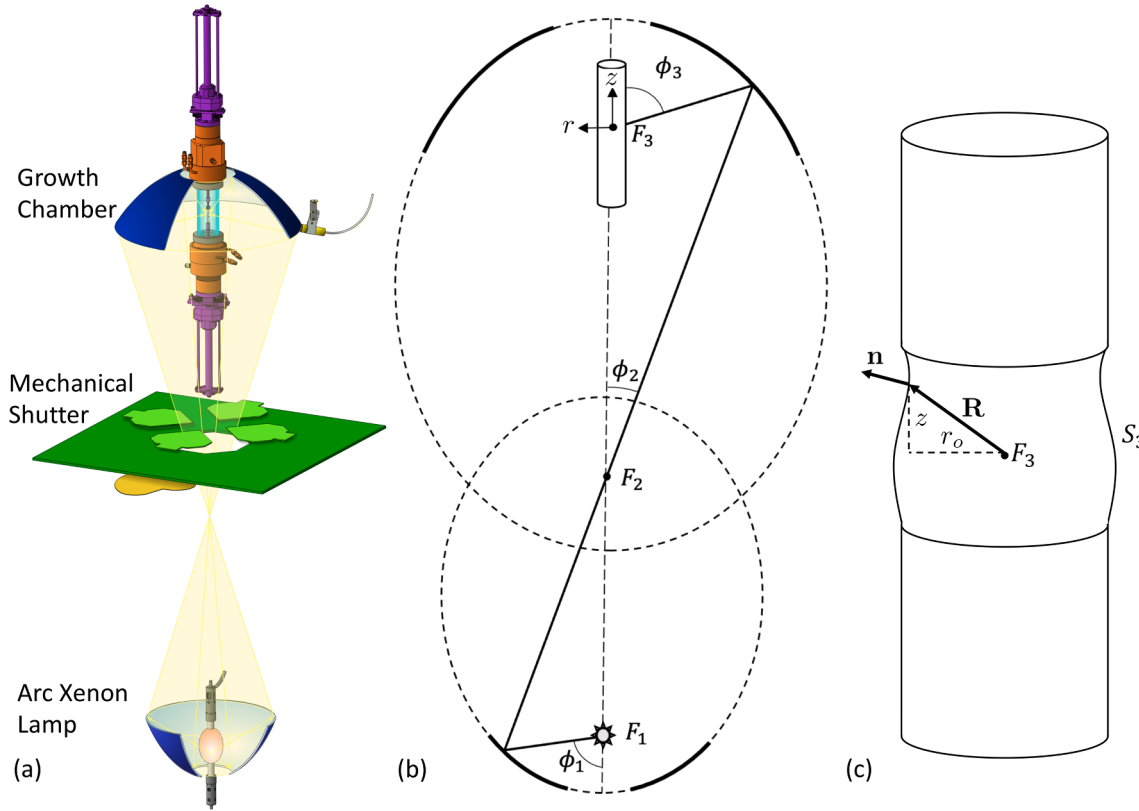


Fig. 3. (a) Schematic diagram of the entire optical system, including the shutter used to control the amount of light entering into the growth chamber (reproduced with permission [15]). Mathematical variables describing (b) the optics of the single-lamp, two-mirror heating system and (c) the geometry of the outer sample surface, S_3 , with respect to focal point F_3 .

$$-k_i \mathbf{n} \cdot \nabla T|_i = \varepsilon_i I(z) + \sigma_B \varepsilon_i (T^4 - T_\infty^4), \quad (18)$$

where the heating of the sample is provided by the incident flux of optical energy from the lamp to the outer surface of the sample, which is given as $I(z)$, a function of axial position, which is derived below. We

retain the simple form for cooling of the sample surface by radiation to a constant far-field temperature, T_∞ , as represented by the second term on the right-hand-side of the above equation.

The optics and geometry of the HKZ system are depicted in Fig. 3(b) as a vertically oriented, two-mirror configuration with a lamp at the focal point of the lower mirror (F_1), the growth system at the focal point

of the top mirror (F_3), and a shared focal point overlapping for both mirrors (F_2). This geometry is axisymmetric and is described by a cylindrical coordinate system with radial and axial components r and z , respectively, whose origin is located at F_3 . Following the prior analyses of Hart [62] and Souptel et al. [63], we assume only primary reflections, consider the mirrors to be perfectly reflecting, and approximate the lamp as an isotropic point source.

Given the three positions of the focal points, the intensity at the focal point located within the sample, F_3 , due to the lamp intensity at F_1 can be calculated. Because the lamp is isotropic, its intensity is given by,

$$I_1 = \frac{P_0}{4\pi}, \quad (19)$$

where I_1 is the power per solid angle around F_1 and P_0 is the lamp power. We relate the intensity around F_2 to F_1 , both lying on focal points within an ellipsoid of revolution, by

$$I_2 = \frac{d\Omega_1}{d\Omega_2} I_1. \quad (20)$$

Here, $d\Omega_i$ is the differential section of the solid angle enclosing focal point i . Extending this for the three focal points, we find an expression for the lamp intensity arriving at focal point F_3 ,

$$I_3 = \frac{d\Omega_2}{d\Omega_3} \frac{d\Omega_1}{d\Omega_2} I_1. \quad (21)$$

Focal point F_3 is embedded within the liquid zone during a growth experiment, as depicted in Fig. 3(b) and (c), but knowing the light energy I_3 focussed on this point allows for the derivation of the intensity along an arbitrary area S_3 surrounding F_3 as,

$$I_{S_3}(z) = \frac{d\Omega_3}{dS_3} \frac{d\Omega_2}{d\Omega_3} \frac{d\Omega_1}{d\Omega_2} I_1, \quad (22)$$

where $I_{S_3}(z)$ is the intensity per unit area and with dS_3 denoting the differential area of interest, which is the outer sample surface for our OFZ model.

To evaluate the above expression, we define a spherical coordinate system centered at F_3 , with a radial coordinate, meridional angle, ϕ , defined as the angle relative to the axial direction e_z of the cylindrical coordinate system, and azimuthal angle, γ . The differential solid angle is written in terms of these coordinates as,

$$d\Omega = \sin(\phi)d\phi d\gamma. \quad (23)$$

In this spherical coordinate system, we define the vector \mathbf{R} to represent the outer sample surface, S_3 , as depicted in Fig. 3(c), and then derive,

$$\frac{d\Omega_3}{dS_3} = \frac{\mathbf{n} \cdot \mathbf{e}_R}{R^2}, \quad (24)$$

where \mathbf{n} is the unit vector that is normal to the surface of the sample, \mathbf{e}_R is a unit vector that points in the same direction as \mathbf{R} , and $R = \|\mathbf{R}\|$ is the magnitude of this surface representation vector. We note that this magnitude can be expressed in terms of the cylindrical coordinates, namely $R = \sqrt{r_o^2 + z^2}$, where the subscript o refers to the outer sample surface; again, refer to Fig. 3(c). Then, the lamp intensity per unit area on the surface of the sample is given by,

$$I_{S_3}(z) = \frac{\mathbf{n} \cdot \mathbf{e}_R}{R^2} \frac{\sin\phi_1}{\sin\phi_3} \frac{d\phi_1}{d\phi_3} I_1, \quad (25)$$

where ϕ_i is the angle at which the light ray passes through focal point i relative to \mathbf{e}_z .

We can further simplify this expression using the relations between angle of incidences, ϕ_i , for an elliptical mirror that were derived by Hart [62] to arrive at,

$$I_{S_3}(z) = \frac{P_0}{4\pi r_o^2} \frac{\sin\phi_1}{\sin\phi_3} \frac{d\phi_1}{d\phi_3} \sin^2\phi_3 (\mathbf{n} \cdot \mathbf{e}_R), \quad (26)$$

where r_o denotes the radial position of the outer sample surface at axial position z and the relations between ϕ_1 , the angle of light emitted from the mirror and ϕ_3 , the angle of incidence on the crystal, are given by

$$\frac{\sin\phi_1}{\sin\phi_3} \frac{d\phi_1}{d\phi_3} = \frac{(1 - e_1^2)(1 + e_1^2 + 2e_1 \cos\phi_1)}{(1 - e_1^2)(1 + e_1^2 + 2e_2 \cos\phi_3)} \quad (27)$$

$$\cos\phi_1 = \frac{(1 + e_1^2)\cos\phi_2 - 2e_1}{1 + e_1^2 - 2e_1 \cos\phi_2} \quad (28)$$

$$\cos\phi_2 = \frac{(1 + e_2^2)\cos\phi_3 - 2e_2}{1 + e_2^2 + 2e_2 \cos\phi_3} \quad (29)$$

$$\cos\phi_3 = \frac{z - z_f}{\sqrt{(z - z_f)^2 + (r_o - r_f)^2}}. \quad (30)$$

Here, r_f and z_f denote the coordinates of the focal point F_3 and e_1 and e_2 are the eccentricities of the lower and upper ellipsoidal mirrors, respectively. The eccentricity of an ellipse is defined as $e = c/a$, with c denoting distance of the focus from the center of the ellipse and a representing the distance of the end of the ellipse from its center.

While the above expression provides the general form of incident radiation on the surface sample, we also need to consider photons that are blocked by the finite extent of the elliptical mirrors and the mechanical shutter. We represent this by limiting the irradiation to a finite region defined by,

$$r_o \cot\phi_{\min} < z < r_o \cot\phi_{\max}, \quad (31)$$

or equivalently

$$\phi_{\min} < \phi_3 < \phi_{\max}. \quad (32)$$

Here, r_o is the radial coordinate of the outer sample surface, ϕ_{\min} is the angle between \mathbf{e}_z and the line connecting F_3 to the highest point of the upper mirror, and ϕ_{\max} is the similarly defined for the lowest part of the upper mirror. The lower limit, ϕ_{\max} , can be further reduced by restricting the shutter opening.

The final form of the irradiation profile supplied to the surface heat flux condition, eq. (18), is,

$$I(z) = \begin{cases} I_{S_3}(z), & \text{when } r_o \cot\phi_{\min} < z < r_o \cot\phi_{\max}, \\ 0, & \text{otherwise.} \end{cases} \quad (33)$$

We plot both the continuous and discontinuous irradiation profiles along the surface of a 6 mm-diameter cylinder, corresponding to $I_{S_3}(z)$ of Eq. (26) and $I(z)$ of Eq. (33), respectively, as functions of axial distance in Fig. 4(a). We note that the actual form of $I(z)$ applied in the new boundary condition, Eq. (18), is computed for the more complicated rod and meniscus geometry of the real system and will differ slightly from the profile for the simple cylinder shown in Fig. 4(a). The asymmetry with respect to the axial position is evident by the skewing of both profiles upward from the focal point. Even more important are the strict cut-off limits to the actual irradiation profile, $I(z)$, that are imposed by the finite range of angles available for the sample to receive power from the lamp.

3.2. Irradiation results and implementation issues

In this and subsequent sections, we compute results for a model system of sapphire crystal growth in the single-lamp, two-mirror optical floating zone furnace. We consider the feed rod and crystal to be 6 mm in diameter and set the translation rate to 0.526 cm/hr. All other physical properties and operating parameters for our calculations are listed in

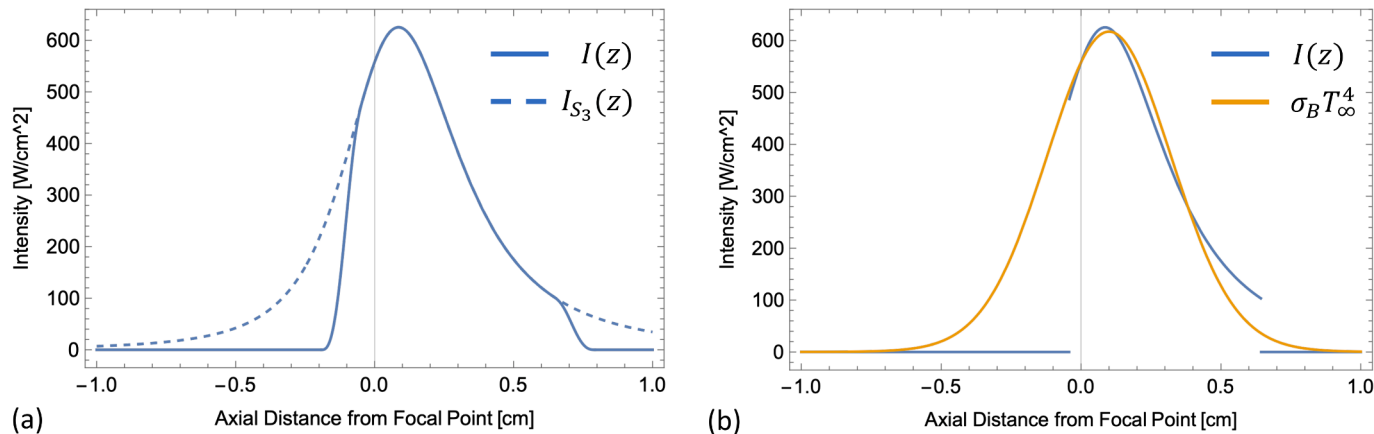


Fig. 4. Irradiation intensity profiles are plotted versus axial distance for a cylindrical surface with a diameter of 6 mm. (a) The dashed curve shows the continuous profile $I_{S_3}(z)$ obtained for uninterrupted mirrors. The solid curve, $I(z)$, is finite only within mirror cut-off limits and is used for subsequent heat transfer calculations. Here, the discontinuities of $I(z)$ are smoothed, as discussed in Section 3.2.2. (b) The discontinuous irradiation profile $I(z)$ is compared with the radiation power, $\sigma_B T_\infty^4$, from a Gaussian far-field temperature profile, $T_\infty(z)$, constructed to mimic the lamp output, as used in Section 3.2.1.

Table 1
Physical Properties of sapphire (Al_2O_3 , from [64]) and system parameters.

Melting Temperature [K]	$T_m = 2323.15$	
Density [g/cm ³]	$\rho_\ell = 3.0$	$\rho_s = 3.96$
Heat Capacity [J/g K]	$C_{p,\ell} = 1.3$	$C_{p,s} = 1.56$
Thermal Conductivity [W/cm K]	$k_\ell = k_s = 3.5 \times 10^{-2}$	
Emissivity	$\varepsilon_\ell = 0.3$	$\varepsilon_s = 1.0$
Thermal Expansion Coefficient [1/K]	$\beta_\ell = 1.8 \times 10^{-5}$	
Latent Heat of Fusion [J/g]	$\Delta H = 1100$	
Surface Tension [dyn/cm]	$\sigma = 360 - 0.035(T - T_m)$	
Viscosity [g/cm s]	$\mu_\ell = 0.475$	
Contact Angle	$\theta_g = 8^\circ$	
Eccentricity (Lower Mirror)	$e_1 = 396/470$	
Eccentricity (Upper Mirror)	$e_2 = 504/655$	
Maximum Intensity Angle Cutoff	$\phi_{\max} = 98^\circ$	
Minimum Intensity Angle Cutoff	$\phi_{\min} = 25^\circ$	
Maximum Profile Temperature [K]	$T_{\max} = 2870$	
Ambient Temperature [K]	$T_0 = 298.15$	
Profile Width [cm]	$\sigma_G = 0.6$	

Table 1.

In all figures of this section, we show the flow field in the melt on the left side of each image by plotting 16 streamfunction contours that are evenly spaced between the maximum and minimum streamfunction values, ψ_{\max} and ψ_{\min} , which are listed in each figure caption. Positive streamfunction values indicate clockwise circulation, negative values correspond to counterclockwise flows. The temperature field is plotted on the right half of each image by isotherms that are chosen with a constant spacing that yields 5 contours in the melt, ranging from the melting temperature at the melt-solid interfaces to a maximum temperature along the meniscus. Color scales are indicated for streamfunction and temperature values in each figure.

3.2.1. Irradiation versus Gaussian profile

To examine the importance of the rigorous irradiation profile on zone heating, we compare a growth simulation using a simple Gaussian profile with the heat flux boundary condition described by Eq. (3) to a calculation that employs the discontinuous irradiation profile derived in the previous section, $I(z)$, in the heat flux boundary condition, Eq. (18). It is important to note that there is no obvious approach to choose the parameters associated with the Gaussian profile, especially if the irradiation profile is not known a priori. Here, we choose the Gaussian profile so that $\sigma_B T_\infty^4$ closely matches the peak power and width of the rigorous irradiation profile for a cylindrical sample of 6 mm diameter. We make no attempt to account for irradiation discontinuities in the

Gaussian profile. Both profiles are shown in Fig. 4(b).

Fig. 5(a) shows the system heated by the Gaussian profile, while (b) shows the same system heated via the irradiation profile of the HKZ furnace. Clearly, these two predictions are very different. The zone length of the case computed with the Gaussian profile is much longer, since the total optical energy delivered to the sample is much larger than the energy provided by the rigorous irradiation profile, which is cut-off by the mirror limits.

Perhaps less obvious but quite important is the axial asymmetry of the system computed for the detailed irradiation profile, shown in Fig. 5 (b). The cut-offs in the irradiation profile result in more power delivered above the focal point and a larger discontinuity below the focal point. The asymmetry in heating makes the upper vortex in the zone much larger than the lower vortex. The Gaussian profile produces upper and lower zone flows that are nearly similar in strength, with the lower vortex being somewhat stronger due to the outward-sagging lower meniscus shape, as shown in Fig. 5(a). Finally, the axial temperature profiles are much more symmetric above and below in the system heated via the Gaussian profile, whereas the detailed irradiation profile produces smaller axial thermal gradients above and larger axial gradients below.

3.2.2. Irradiation profile discontinuities

The discontinuous irradiation profile, $I(z)$, appearing in the OFZ boundary condition, Eq. (18), causes step changes in the heat flux along the outer sample surface. These discontinuities do not make the governing equations mathematically ill-posed; however, they do result in solutions that display very large temperature gradients localized around the irradiation discontinuities. Accurate resolution of these steep gradients requires fine spatial discretization via small elements. In our OFZ model, these elements shift in space with each iteration as the locations of the free boundaries are updated, making convergence of this nonlinear model exceedingly difficult. We discuss below two methods to effectively accommodate the discontinuities in the heat flux boundary condition.

In our first approach, we take advantage of an important feature of the Galerkin finite element method and its weak form [46–49]. By construction, the basis functions that are defined over the elements ensure continuity of the temperature field everywhere, but the first derivatives of these basis functions (representing the temperature gradient) are discontinuous between adjacent elements. It is then the weak form of the discretized governing equations that enforces the continuity of heat flux between adjacent elements. Because of this feature of representation in the Galerkin finite element method,

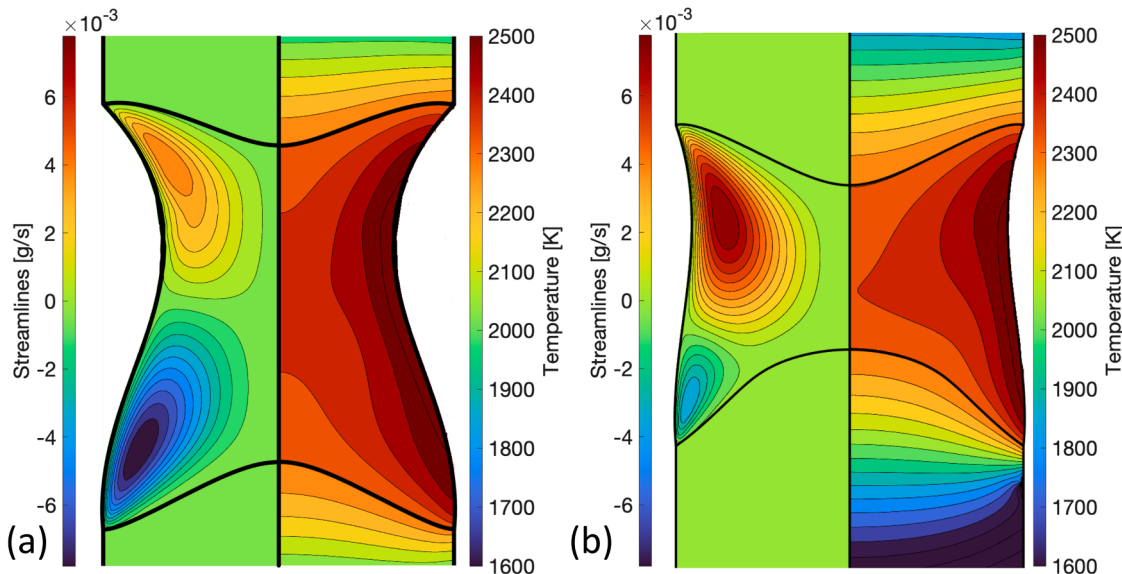


Fig. 5. Streamlines and temperature contours are plotted for (a) zone heating via a Gaussian far-field temperature profile ($\psi_{max} = 0.004561$ g/s, $\psi_{min} = -0.007788$ g/s, $T_{max} = 2617$ K) and (b) zone heating by HKZ irradiation profile ($\psi_{max} = 0.0079$ g/s, $\psi_{min} = -0.0035$ g/s, $T_{max} = 2601.8$ K).

discontinuous heat flux boundary conditions are readily accommodated when the jump occurs exactly at an element edge. Following this logic, we construct our OFZ mesh so that the irradiation discontinuities lie at element edges.

We applied this approach to compute the sapphire growth solution previously shown in Fig. 5b) and reproduced in Fig. 6(a). Despite the fidelity of this approach in representing the discontinuities in irradiation, its implementation still proves challenging. Specifically, we immobilize small sections of the mesh to keep the discontinuities of the irradiation profile at element edges; however, since these regions are so close to the unknown melt-solid interfacial free boundaries, mesh movement between iterations can produce excessive element distortion. This approach then required substantial trial and error and frequent tuning of the Newton iteration steps to avoid mesh tangling and solution divergence.

An alternative, more pragmatic approach is to smooth the irradiation profile in a manner that improves convergence without unduly affecting the resulting solution. We implement this idea using polynomials defined over small intervals to replace the cut-off discontinuities, resulting in a smooth irradiation profile, which is then normalized to match the integrated power of the original profile. The details of the profile modification are provided in [65], and Fig. 4(a) shows an irradiation profile using smoothing intervals of 1 mm width.

Fig. 6 shows growth states computed using the discontinuous irradiation profile, shown as (a), and the smoothed irradiation profile of Fig. 4(a) in (b), keeping all other parameters the same. The largest difference between these cases is in the axial temperature profiles below the liquid zone, where smoothing the discontinuous irradiation results in lower gradients in (b) compared to (a). However, other measures of the two solutions are more similar. The flow strength of the lower vortex

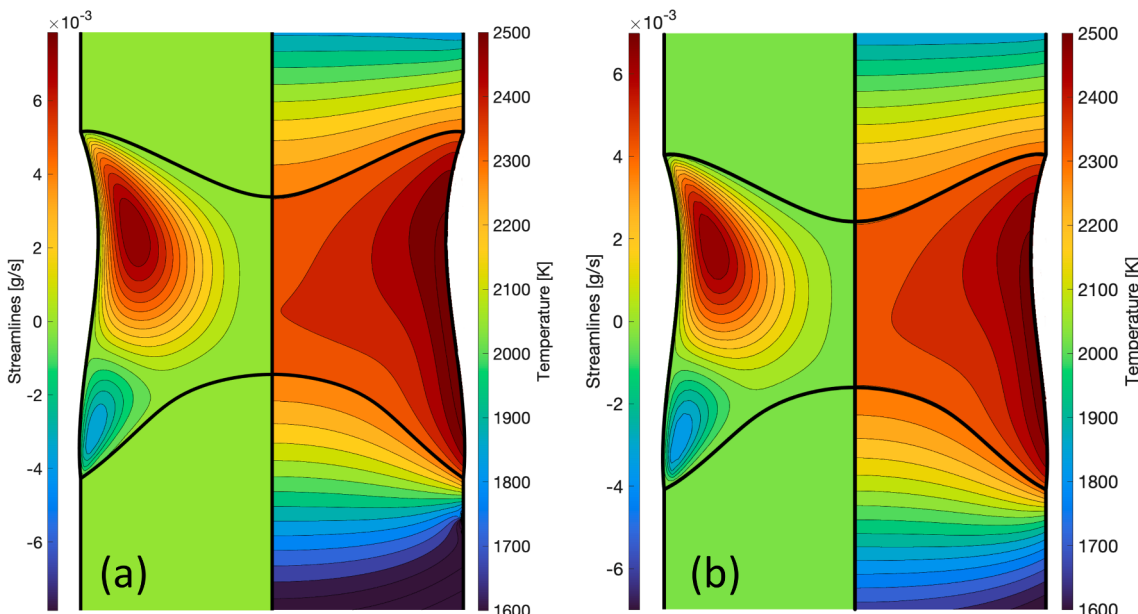


Fig. 6. Streamlines and temperature contours are plotted for (a) discontinuous irradiation profile ($\psi_{max} = 0.0079$ g/s, $\psi_{min} = -0.0035$ g/s, $T_{max} = 2601.8$ K) and (b) irradiation profile with smoothed discontinuities ($\psi_{max} = 0.007$ g/s, $\psi_{min} = -0.0035$ g/s, $T_{max} = 2563.1$ K).

is unchanged in both cases, but the total circulation of the upper vortex decreases by 11.4% in the smoothed case. This is consistent with a decrease in the maximum temperature (occurring along the melt meniscus) of 1.5% for case computed with the smoothed irradiation profile.

4. Gas phase model

The high-pressure optical floating zone furnace was specifically developed to access a much richer phase space for materials discovery [2–4,6–11,5]. However, growth experiments under extremely high pressures have led to unexpected growth behaviors [3,5]. Here, we explicitly model the effects of pressure on the atmosphere surrounding the sample in the HKZ furnace. We incorporate flow and heat transfer equations for the gas phase within our thermal-capillary model and thus are able to consider their effects on all free boundaries, unlike prior implementations to model gas-phase flows in floating zone systems [34–37].

4.1. Governing equations

We compute the steady-state temperature field in the surrounding gas phase by applying the previously presented energy balance, Eq. (1), over the additional gas/fluid domain depicted in Fig. 1(b). The temperature field and heat fluxes are continuous between the sample and the surrounding gas phase, and these conditions are naturally enforced via the Galerkin finite element method. In particular, the heat fluxes between the outer sample surface and the surrounding gas phase are now represented as,

$$-k_i \mathbf{n} \cdot (\nabla T|_i - \nabla T|_g) = \varepsilon_i I(z) + \sigma_B \varepsilon_i (T^4 - T_\infty^4), \quad (34)$$

where \mathbf{n} is a unit vector pointing outward from and normal to the sample outer surface. Along the outermost radial boundary of the gas phase, where the gas meets the enclosure wall, we impose a far-field radiative cooling condition,

$$-k_g \mathbf{e}_r \cdot \nabla T|_g = \sigma_B \varepsilon_e (T^4 - T_\infty^4), \quad (35)$$

where ε_e denotes the emissivity of the enclosure surface. Finally, we approximate heat transfer along the upper surfaces of the growth chamber by applying no-flux conditions,

$$\mathbf{e}_z \cdot \nabla T|_g = 0. \quad (36)$$

We describe flows in the surrounding gas phase via the same Navier–Stokes equations, Eqs. (7)–(9), employed to describe flow in the liquid zone. Over the new gas domain, we impose no-flow conditions of $\mathbf{u}_g = \mathbf{0}$ along the inner wall of the growth chamber, where \mathbf{u}_g denotes the velocity of the gas/fluid phase. No-slip conditions are also applied along the feed rod and crystal outer surfaces as,

$$\mathbf{u}_g = \mathbf{u}_s = u_s \mathbf{e}_z, \quad (37)$$

where \mathbf{u}_s is the prescribed rod translation rate. We next modify the force balance applied along the melt meniscus, Eq. (12), to include the effects of the gas phase as,

$$\mathbf{n} \cdot (\mathbf{T}|_\ell - \mathbf{T}|_g) = 2\mathcal{H}\sigma\mathbf{n} + \nabla_s \sigma, \quad (38)$$

and complete the flow field specifications by applying a tangential no-slip condition between the flow field in the liquid zone and the surrounding gas,

$$\mathbf{t} \cdot (\mathbf{u}_\ell - \mathbf{u}_g) = 0. \quad (39)$$

We note that the equations describing the free boundaries in the system

remain unchanged from the thermal-capillary base model, except that the kinematic condition applied along the melt meniscus, Eq. (16), now includes the non-zero gas-phase velocity, \mathbf{u}_g .

It is appropriate to assess the validity of describing flows in the surrounding atmosphere using the same form of the Navier–Stokes equation as applied to model flows in the liquid zone. This atmosphere consists of a gas phase for pressures below approximately 50 bars and a supercritical fluid for pressures beyond. First, we assert that the assumption of incompressibility is very good for describing low-Mach-number gas flows in which shock-wave phenomena are unimportant, as is the case for both the gas and supercritical fluid encountered in this system.

Next, we also assert that the Boussinesq approximation is also valid to model the flows in this region. The Boussinesq approximation applies the effects of temperature-dependent density only in the body-force term of the momentum balance, Eq. (7), and is valid as long as density changes are relatively small, namely when $\Delta\rho/\rho \ll 1$, with $\Delta\rho$ depicting the density changes induced by temperature variation. In the low pressure gas phase, $\Delta\rho/\rho_g \approx 10^{-4}$ at 1 bar; however, this ratio becomes larger for the supercritical fluid phase, with $\Delta\rho/\rho_g \approx 0.1$ at 300 bar. To further assess the Boussinesq approximation, Gresho [66] argued that its validity depends upon the rate of nonphysical mass creation that arises from ignoring density variations in the continuity equation. For the high-pressure cases, we estimate that the worst cases for mass conservation errors are less than 1%; more details are provided in [65]. Therefore, we conclude that Eqs. (7)–(9) are appropriately applied to describe the gas and supercritical fluid flows in the high-pressure OFZ system.

The temperature, velocity, and pressure fields of the new gas/fluid domain are solved using the same Galerkin finite element method described previously.

4.2. Gas flows and pressure effects

We consider the effects of pressure on our test system of 6 mm-diameter sapphire crystal growth in an HKZ furnace heated via the vertically oriented dual-mirror setup discussed earlier. The surrounding gas is taken to be pure oxygen at varying pressures between 1–300 bar, which takes the atmosphere from a gas to a supercritical fluid.

While there are profound thermodynamic differences, the distinction between a gas and a supercritical fluid is irrelevant for the low-Mach number flows in the growth chamber. Namely, both behave as incompressible fluids, and the system pressure only affects the values of the transport properties for flow. To simulate different system pressures, we simply apply new values for the fluid density and coefficient of thermal expansion, both of which scale linearly with absolute pressure. We also account for local changes in viscosity with temperature. All physical properties are listed in Table 2, as reported in [67].

Fig. 7 shows streamlines and temperature contours in the zone, feed, and crystal for the growth system under increasing pressures while keeping all other growth parameters constant. Ten streamlines are plotted over all fluid domains, equally spaced between ψ_{max} and ψ_{min} , using the same convention as before, with positive values for clockwise circulation and negative values for counterclockwise flows. On the right

Table 2
Physical Properties of O₂ (from [67]) and chamber parameters.

Density [g/cm ³]	$\rho_g = 0.38 \times 10^{-3} P/P_0, P_0 = 1 \text{ bar}$
Heat Capacity [J/g K]	$C_{pg} = 0.99$
Thermal Conductivity [W/cm K]	$k_g = 4.3 \times 10^{-4}$
Thermal Expansion Coefficient [1/K]	$\beta_g = 2.13 \times 10^{-7} P/P_0$
Viscosity [g/cm s]	$\mu_g = 4.98 \times 10^{-5} + 3 \times 10^{-8}(T - T_m)$
Chamber Height [cm]	$H = 4.5$
Chamber Wall Inner Radius [cm]	$R_w = 3$
Emissivity	$\varepsilon_e = 0.1$

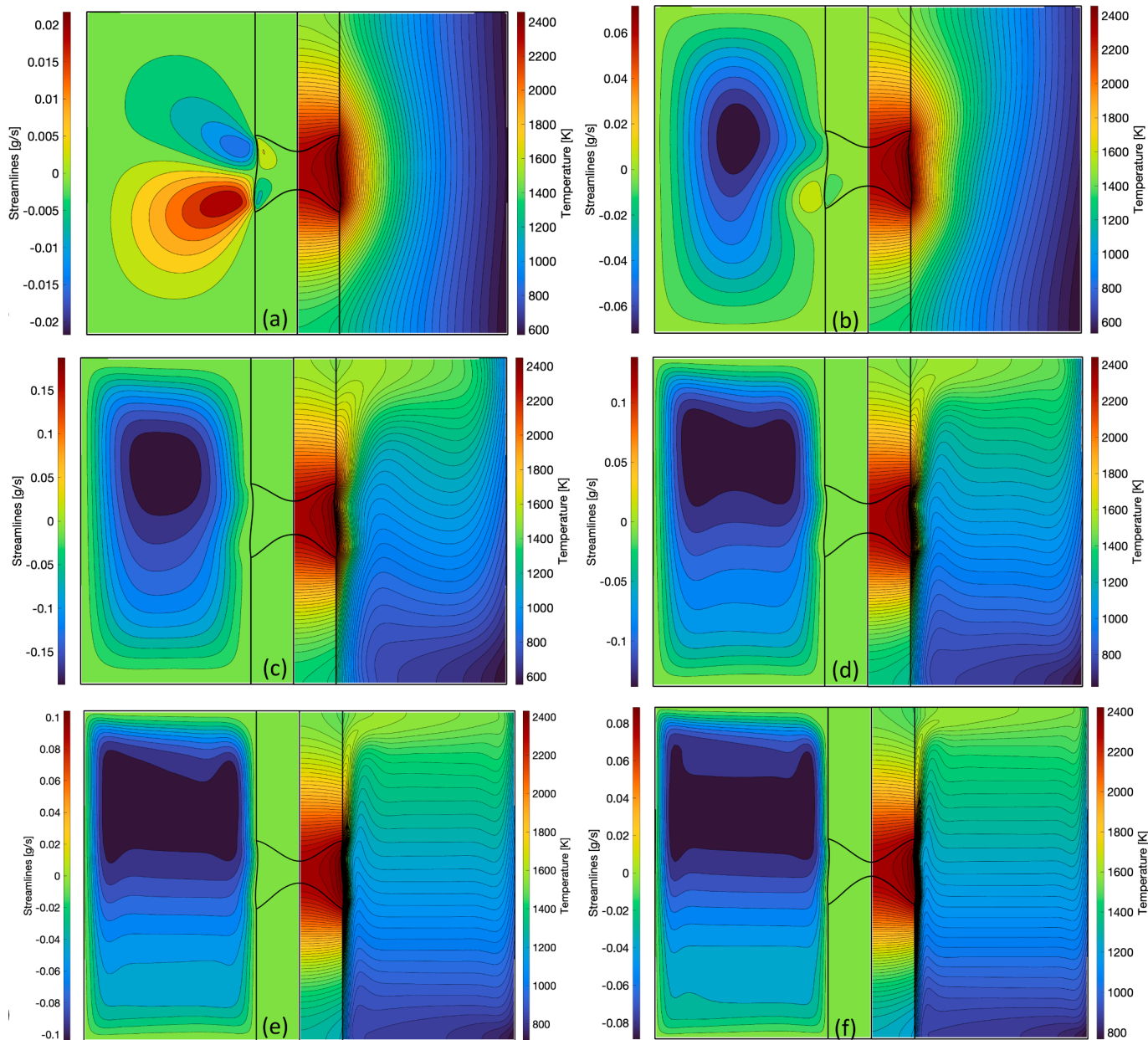


Fig. 7. Streamlines and temperature contours over a range of pressures; (a) 1 bar, (b) 10 bar, (c) 50 bar, (d) 100 bar, (e) 200 bar, and (f) 300 bar.

side of each plot, isotherms are plotted with an equal spacing to give 5 contours in the melt.

The system at a pressure of 1 bar is shown in Fig. 7(a) and is nearly identical to the state predicted by the simpler, thermal-capillary base model shown in Fig. 6. In the surrounding atmosphere, gas flows are primarily driven by tangential forces generated by the Marangoni flows along the melt zone meniscus. As the gas pressure increases, the buoyant flow strengthens and counteracts the lower, clockwise gas-phase vortex, reducing its spatial extent and lessening its convective cooling of the zone. With decreased cooling, the maximum zone temperature increases slightly, which marginally increases the Marangoni flows and the length of the melt zone, an effect that is observed comparing the 1 bar system to the 10 bar system, shown in Figs. 7(a) and (b).

As the pressure is further increased, to 50 bar in Fig. 7(c), the surrounding atmosphere becomes a supercritical fluid; however, the growth characteristics, in terms of the melt zone flow, temperature field, and sample geometry, are similar to those of the 1 bar system. The

effects of buoyancy are increasingly evident as a large vortex fills the growth chamber, flowing upward along the outer sample surface and downward along the chamber wall. At 50 bar, the buoyant flow in the surrounding fluid becomes strong enough to drive significant convective heat transfer, which rearranges the temperature field to exhibit boundary layers and a vertically stratified core [68], as shown on the right of Fig. 7(c).

Figs. 7(d)–(f) show the continued strengthening of the buoyancy-driven flows of the surrounding fluid as the pressure increases up to 300 bar, the upper limit achievable in the current HKZ furnace, with boundary layers becoming evident along the outer surface of the sample and the inner walls of the growth chamber. With increasing pressure, the boundary layers become thinner and the core becomes more vertically stratified, exhibiting nearly flat streamlines and isotherms.

Significantly, the effects of these buoyant flows on crystal growth become increasingly more important as the system pressure is increased. Convective cooling of the sample increases with the stronger gas/fluid flows at higher pressures, resulting in melt zones that become shorter

and melt-solid interfaces that become more deflected. The flows within the melt zone also weaken as the meniscus is increasingly cooled by the flow of the surrounding fluid.

The driving force for these buoyant flows is quantified by a dimensionless Grashof number defined as,

$$\text{Gr} = \frac{\rho_0^2 g \beta \Delta T D^3}{\mu^2}, \quad (40)$$

where ΔT is the temperature difference measured between the hottest point on the meniscus surface to the opposing enclosure wall and $D = R_w - R$ is the annular width within the enclosure, with R_w representing the inner radius of the enclosure wall and R denoting the radius of the feed rod and crystal. Noting that both the fluid density, ρ_0 , and thermal expansion coefficient, β , are linearly proportional to pressure, we expect the Grashof number should scale with pressure as,

$$\text{Gr} \sim \rho_0^2 \beta \sim \left(\frac{P}{P_0}\right)^3, \quad (41)$$

where P_0 represents one atmosphere, as long as the temperature differential across the chamber, ΔT , does not substantially change. Fig. 8(a) shows that the Grashof number in the gas/fluid phase nearly perfectly follows the above scaling with system pressure.

Furthermore, we know from dominant-balance arguments [68,66,69] that the strength of the gas/fluid flow should scale with the buoyancy driving force as,

$$\text{Re} \sim \text{Gr}^{1/2} \sim \left(\frac{P}{P_0}\right)^{3/2}, \quad (42)$$

where the dimensionless Reynolds number is given by $\text{Re} \equiv \rho_0 v_{max} D / \mu$, with v_{max} denoting the maximum velocity of the flow.

Fig. 8(b) shows two plots of the pressure dependence of the Reynolds number in the gas/fluid phase that are calculated using different characteristic velocities. The solid line represents the Reynolds number calculated using the maximum gas-phase velocity over the entire system. At lower pressures, the maximum velocity in the gas phase occurs along the surface of the meniscus, where the gas is dragged along by the strong, Marangoni flows of the melt zone, as is apparent in Figs. 7(a) and (b). The slope of the curve in this pressure regime is nearly unity and $\text{Re} \sim (P/P_0)$. This scaling primarily reflects the linear dependence of the gas density on pressure, along with the nearly constant Marangoni driving force for the flow. As the pressure continues to increase beyond $P \geq 100$ bar, the buoyancy-dominated scaling of $\text{Re} \sim (P/P_0)^{3/2}$ is approached by this curve, corresponding to the states shown in Figs. 7

(d)–(f).

The effects of Marangoni, drag-driven flows in the gas-phase are bypassed with the data used to plot the dashed curve of Fig. 8(b). This curve employs a Reynolds number that is computed using the maximum velocity found in a region enclosed by the outer chamber wall and an inner boundary, located 2 mm away from the outer sample surface. By excluding gas flows driven by meniscus drag, the maximum velocity in this annulus more faithfully reflects flows driven by buoyancy, and the dashed curve more accurately shows the expected scaling of $\text{Re} \sim (P/P_0)^{3/2}$ from Eq. (42).

For the stronger buoyant flows corresponding to higher pressures, we observe the formation of boundary layers and a vertically stratified core, similar to the case studied by Gill [68] of natural convection in a horizontal cavity. To examine these boundary layers, axial velocity and temperature are plotted as functions of radial position outward from the sample surface, along the axial midline of the system, for system pressures of 50 bar and above in Fig. 9. The dimensional profiles shown in the upper panels, (a) and (b), clearly indicate stronger flows and thinner boundary layers as the pressure increases. Also evident are the lower meniscus temperatures (at $r = 0$) caused by increased convective cooling of the melt zone at higher pressures. The lower plots, (c) and (d), plot dimensionless profiles, following the analysis of Gill [68], who predicted that the boundary layer thickness is proportional to $\text{Ra}^{-1/4}$ and that the strength of the vertical flow scales as $\text{Re} \sim \text{Ra}^{1/2}$. Here, the dimensionless Rayleigh number, $\text{Ra} = \text{PrGr}$, is the product of the previously defined Grashof number and the Prandtl number, $\text{Pr} \equiv \mu_g C_{p,g} / k_g$. The scaled profiles show good agreement with the expected behavior of strong, buoyant flows in an enclosure.

5. Conclusions

We have presented a thermal-capillary model describing steady-state crystal growth in the optical floating zone furnace following original formulations of Duranteau and Brown [16] and have validated our model against prior computations of Lan and Kou [19]. We further describe significant extensions to this model via the detailed representation of irradiation heating and enclosure pressure in the single-lamp, two-mirror ScIDre HKZ furnace [15]. These important phenomena have not been considered in prior models of the optical floating zone.

Initial results show the importance of a detailed accounting of irradiation by comparison to results computed using a simple model of Gaussian heating that has been often employed in past studies. Our results show that the appropriate Gaussian heating profile is difficult to choose a priori and does not represent important details of the more

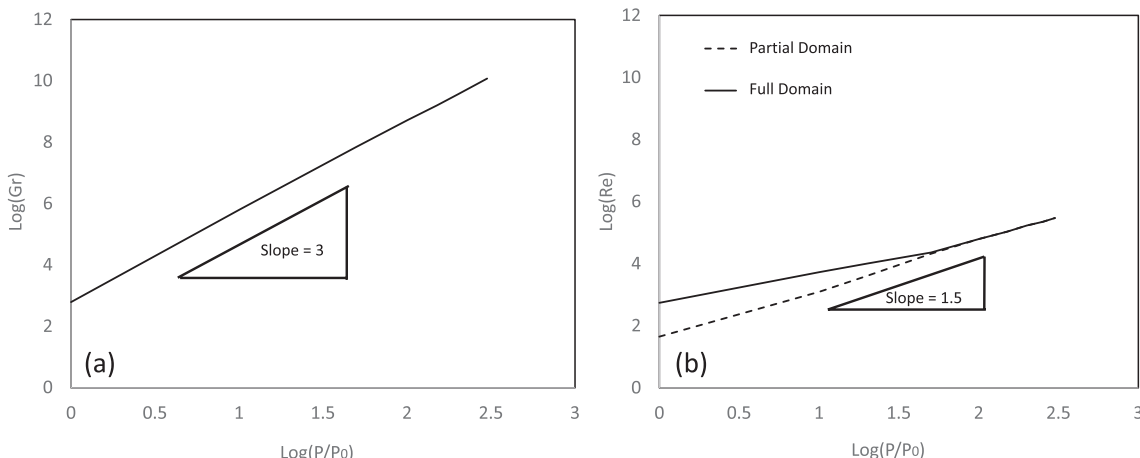


Fig. 8. Log-log plots show measures of the flow in the surrounding atmosphere versus system pressure for (a) the Grashof number, measuring the driving force for buoyant flow, and (b) the Reynolds number, measuring the strength of the gas/fluid flow. The solid curve computes Re using the maximum velocity within the full gas/fluid domain, while the dashed curve uses the velocity from a partial domain that excludes flows near the surface of the sample.

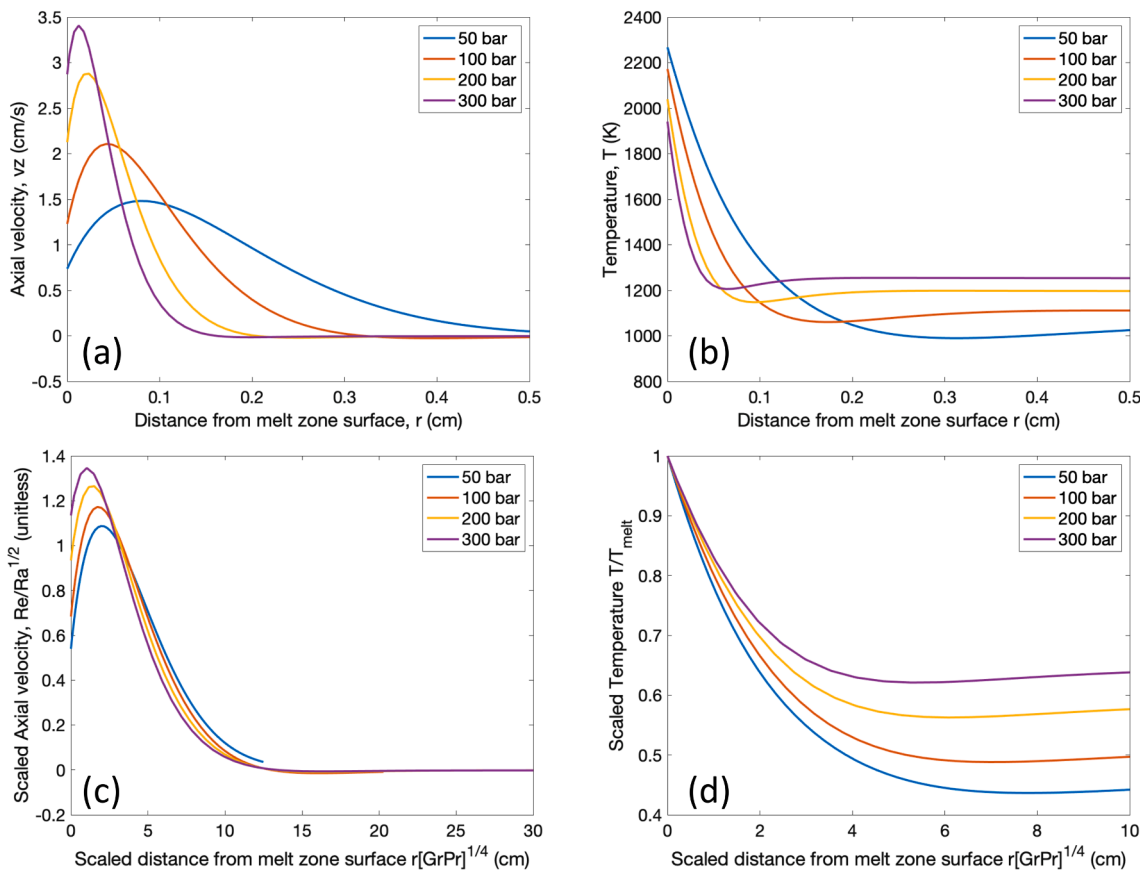


Fig. 9. Axial velocity and temperature are plotted versus radial distance from the sample melt surface, along at the axial center point of the system. Dimensional profiles are shown for a different system pressures in (a) and (b). Dimensionless profiles are plotted in (c) and (d), using scalings for strong, buoyant flows in an enclosure [68].

complicated irradiation profile, such as axial asymmetry and discontinuous cut-offs of the lamp radiation. We also discuss implementation challenges caused by the discontinuities of the irradiation profile. For simulation of the sapphire growth test system considered here, we judged the trade-off between significantly easier convergence versus loss of accuracy to favor the use of the smoothed irradiation profile over other approaches. More details and cases using smoothing are discussed in [65].

Finally, we have presented the first analysis of the effects of pressure on flows in the gas/fluid phase within the growth enclosure using a comprehensive model that accounts for all free boundaries in the OFZ growth system. In particular, we demonstrate that the driving force and strength of buoyant flows in the surrounding fluid phase increase non-linearly with pressure, with the Grashof number scaling as $Gr \sim (P/P_0)^3$ and the Reynolds number scaling as $Re \sim (P/P_0)^{3/2}$. At higher pressures and stronger flows, boundary layers form against the growth sample that are well described by classical analyses of convective flows with an enclosure [68].

The impact of the gas/fluid flows on the growth system are extremely important for pressures of 100 bar and above. Strong convective cooling of the growth sample occurs at higher pressures, leading to significantly shorter melt zones, more deflected melt-solid interfaces, and weaker flows in the zone. At these high pressures, more irradiation power would be needed to maintain zone sizes comparable to those attained under lower pressure operation. For the highest pressure simulated here, 300 bars, we compute a Grashof number of $Gr = 4.2 \times 10^8$, a driving force that is likely high enough to result in turbulent flows in the fluid phase surrounding the sample, which is consistent with observations by Phelan et al. [5]. Cumulatively, these predicted behaviors are consistent with prior reports of stable growth being more difficult to maintain at high

system pressures [3,5].

While we believe that these modeling advances are significant, there are additional features that may be needed to accurately describe OFZ growth in these systems. In particular, the faithful accounting of radiation heat transfer is expected to be important, requiring the application of radiation enclosure analysis in general [70,71,40] and the consideration of internal radiation in particular [72–76,40] to describe crystals that exhibit significant transparency to infrared wavelengths, such as many oxides [1].

Towards such future developments, we cite the 2009 National Resource Council report, *Frontiers in Crystalline Matter: From Discovery to Technology*, in which Robert Cava of Princeton University stated, from a materials discovery point of view, that floating zone techniques are “arguably the best thing to happen to single-crystal growth in the past 25 years” [77]. We assert that the advances in fundamental understanding of OFZ promoted by models such as those described here will make these systems even better for single crystal growth.

Declaration of Competing Interest

The authors declare that they have no known competing financial interests or personal relationships that could have appeared to influence the work reported in this paper.

Acknowledgments

We acknowledge assistance from the entire Goma team at the University of New Mexico, particularly Andrew Cochrane, for insight and helpful discussions. We thank Hanna Dabkowska (McGill University) and John Mitchell (Argonne National Laboratory) for initial advice and

encouragement. SSD would like to thank Scientific Instruments Dresden GmbH (SciDre) for support to attend the 3rd Workshop on the Floating Zone Technique, Oxford University, September 16–18, 2019.

References

- [1] H. Dabkowska, A. Dabkowski, Optical floating zone—Complementary crystal growth technique for new classes of oxide materials, in: P. Rudolph (Ed.), Bulk Crystal Growth: Basic Techniques, Handbook of Crystal Growth, second ed., vol. IIA, Elsevier, 2015, pp. 283–312 (Chapter 8.1).
- [2] Basic Research Needs for Synthesis Science, Report of the Basic Energy Sciences Workshop on Synthesis Science for Energy Relevant Technology, Tech. rep., Department of Energy Basic Energy Sciences (2016).
- [3] J.F. Mitchell, High pressure floating zone growth of correlated electron oxides, presentation at 21st American Conference on Crystal Growth and Epitaxy (ACCGE-21), Santa Fe, NM (July 30–August 4, 2017).
- [4] D. Sedmidubský, V. Jakes, O. Jankovský, J. Leitner, Z. Sofer, J. Hejtmanek, Phase equilibria in Ca–Co–O system, *J. Solid State Chem.* 194 (2012) 199–205, <https://doi.org/10.1016/j.jssc.2012.05.014>. URL: <http://www.sciencedirect.com/science/article/pii/S0022459612003271>.
- [5] W.A. Phelan, J. Zahn, Z. Kennedy, T.M. McQueen, Pushing boundaries: High pressure, supercritical optical floating zone materials discovery, *J. Solid State Chem.* 270 (December 2018) (2019) 705–709. <https://doi.org/10.1016/j.jssc.2018.12.013>.
- [6] J. Zhang, H. Zheng, C.D. Malliakas, J.M. Allred, Y. Ren, Q.L.Q., T.-H.Han, J.F. Mitchell, Brownmillerite $\text{Ca}_2\text{Co}_2\text{O}_5$: Synthesis, stability, and re-entrant single crystal to single crystal structural transitions, *Chem. Mater.* 26(24) (2014) 7172–7182.
- [7] F. Cansell, B. Chevalier, A. Demourgues, J. Etourneau, C. Even, Y. Garrabos, V. Pessey, S. Petit, A. Tressaud, F. Weill, Supercritical fluid processing: A new route for materials synthesis, *J. Mater. Chem.* 9 (167–75) (1999).
- [8] M. Hasegawa, T. Yagi, Systematic study of formation and crystal structure of 3d-transition metal nitrides synthesized in a supercritical nitrogen fluid under 10 GPa and 1800 K using diamond anvil cell and YAG laser heating, *J. Alloy. Compd.* 403 (1–2) (2005) 131–142.
- [9] M. Brasse, L. Chioncel, J. Kune, A. Bauer, A. Regnat, C.G.F. Blum, S. Wurmehl, C. Pfleiderer, M.A. Wilde, D. Grundler, de Haas-van Alphen effect and Fermi surface properties of single-crystal CrB_2 , *Phys. Rev. B* 88 (15) (2013) 155138.
- [10] H.B. Cao, Z.Y. Zhao, M. Lee, E.S. Choi, M.A. McGuire, B.C. Sales, H.D. Zhou, J.-Q. Yan, D.G. Mandrus, High pressure floating zone growth and structural properties of ferrimagnetic quantum paraelectric $\text{BaFe}_{12}\text{O}_{19}$, *APL Mater.* 3 (6) (2015) 062512.
- [11] Z.W. Li, C.F. Liu, M. Skoulatos, L.H. Tjeng, A.C. Komarek, Floating zone growth of Ba-substituted ruthenate $\text{Sr}_{2-x}\text{Ba}_x\text{RuO}_4$, *J. Cryst. Growth* 427 (2015) 94–98.
- [12] J. Zhang, H. Zheng, Y. Ren, J. Mitchell, High pressure floating-zone growth of perovskite nickelate LaNiO_3 single crystals, *Cryst. Growth Design* 17 (5) (2017) 2730.
- [13] N. Schreiber, J. Zhang, H. Zheng, J. Freeland, Y.-S. Cheng, J. Mitchell, D. Phelan, Single crystal growth and structural evolution across the 1st order valence transition in $(\text{Pr}_{1-y}\text{Y}_{y})_{1-x}\text{Ca}_x\text{CoO}_{3-\delta}$, *J. Solid State Chem.* 254 (2017) 69–74.
- [14] H. Li, X. Zhou, T. Nummy, J. Zhang, V. Pardo, W.E. Pickett, J. Mitchell, D. Dessau, Fermiology and electron dynamics of trilayer nickelate $\text{La}_4\text{Ni}_3\text{O}_{10}$, *Nat. Commun.* 8 (2017) 704.
- [15] SciDre, Scientific Instruments Dresden GmbH. URL: <http://scidre.de/index.php>.
- [16] J.L. Duranteau, R.A. Brown, Thermal-capillary analysis of small-scale floating zones: Steady-state calculations, *J. Cryst. Growth* 75 (1986) 367–389.
- [17] C. Lan, S. Kou, Thermocapillary flow and melt/solid interfaces in floating-zone crystal growth under microgravity, *J. Cryst. Growth* 102 (4) (1990) 1043–1058, [https://doi.org/10.1016/0022-0248\(90\)90873-J](https://doi.org/10.1016/0022-0248(90)90873-J). URL: <http://www.sciencedirect.com/science/article/pii/S002202489090873J>.
- [18] C. Lan, Y. Kim, S. Kou, A half-zone study of Marangoni convection in floating-zone crystal growth under microgravity, *J. Cryst. Growth* 104 (4) (1990) 801–808, [https://doi.org/10.1016/0022-0248\(90\)90105-T](https://doi.org/10.1016/0022-0248(90)90105-T). URL: <http://www.sciencedirect.com/science/article/pii/S002202489090105T>.
- [19] C.W. Lan, S. Kou, Heat transfer, fluid flow and interface shapes in floating-zone crystal growth, *J. Cryst. Growth* 108 (1–2) (1991) 351–366, [https://doi.org/10.1016/0022-0248\(91\)90383-G](https://doi.org/10.1016/0022-0248(91)90383-G).
- [20] C. Lan, S. Kou, Effects of rotation on heat transfer, fluid flow and interfaces in normal gravity floating-zone crystal growth, *J. Cryst. Growth* 114 (4) (1991) 517–535, [https://doi.org/10.1016/0022-0248\(91\)90397-N](https://doi.org/10.1016/0022-0248(91)90397-N). URL: <http://www.sciencedirect.com/science/article/pii/S002202489190397N>.
- [21] C. Lan, S. Kou, Effect of rotation on radial dopant segregation in microgravity floating-zone crystal growth, *J. Cryst. Growth* 133 (3) (1993) 309–321, [https://doi.org/10.1016/0022-0248\(93\)90170-2](https://doi.org/10.1016/0022-0248(93)90170-2). URL: <http://www.sciencedirect.com/science/article/pii/S0022024893901702>.
- [22] C. Lan, S. Kou, Formulation for correcting optical distortions due to a transparent floating zone, *J. Cryst. Growth* 132 (3) (1993) 471–476, [https://doi.org/10.1016/0022-0248\(93\)90074-7](https://doi.org/10.1016/0022-0248(93)90074-7). URL: <http://www.sciencedirect.com/science/article/pii/S0022024893900747>.
- [23] C. Lan, S. Kou, Radial dopant segregation in zero-gravity floating-zone crystal growth, *J. Cryst. Growth* 132 (3) (1993) 578–591, [https://doi.org/10.1016/0022-0248\(93\)90085-B](https://doi.org/10.1016/0022-0248(93)90085-B). URL: <http://www.sciencedirect.com/science/article/pii/S002202489390085B>.
- [24] C.W. Lan, Newton's method for solving heat transfer, fluid flow and interface shapes in a floating molten zone, *Int. J. Numer. Meths. Fluids* 19 (1994) 41–65.
- [25] C. Lan, Heat transfer, fluid flow, and interface shapes in the floating-zone growth of tube crystals, *J. Cryst. Growth* 141 (1) (1994) 265–278, [https://doi.org/10.1016/0022-0248\(94\)90120-1](https://doi.org/10.1016/0022-0248(94)90120-1). URL: <http://www.sciencedirect.com/science/article/pii/0022024894901201>.
- [26] C. Lan, Thermal-capillary analysis of floating-zone growth of tube crystals: steady-state and conduction dominated calculations, *J. Cryst. Growth* 135 (3) (1994) 606–618, [https://doi.org/10.1016/0022-0248\(94\)90154-6](https://doi.org/10.1016/0022-0248(94)90154-6). URL: <http://www.sciencedirect.com/science/article/pii/0022024894901546>.
- [27] C.W. Lan, C.H. Tsai, Modeling of ellipsoid mirror furnace for floating-zone crystal growth, *J. Cryst. Growth* 173 (3–4) (1997) 561–573, [https://doi.org/10.1016/S0022-0248\(96\)00971-2](https://doi.org/10.1016/S0022-0248(96)00971-2).
- [28] C. Lan, M. Liang, Modulating dopant segregation in floating-zone silicon growth in magnetic fields using rotation, *J. Cryst. Growth* 180 (3) (1997) 381–387, [https://doi.org/10.1016/S0022-0248\(97\)00264-9](https://doi.org/10.1016/S0022-0248(97)00264-9). URL: <http://www.sciencedirect.com/science/article/pii/S0022024897002649>.
- [29] C. Lan, J. Chian, Three-dimensional simulation of Marangoni flow and interfaces in floating-zone silicon crystal growth, *J. Cryst. Growth* 230 (1) (2001) 172–180, [https://doi.org/10.1016/S0022-0248\(01\)01328-8](https://doi.org/10.1016/S0022-0248(01)01328-8). URL: <http://www.sciencedirect.com/science/article/pii/S0022024801013288>.
- [30] C. Lan, Three-dimensional simulation of floating-zone crystal growth of oxide crystals, *J. Cryst. Growth* 247 (3) (2003) 597–612, [https://doi.org/10.1016/S0022-0248\(02\)02056-0](https://doi.org/10.1016/S0022-0248(02)02056-0). URL: <http://www.sciencedirect.com/science/article/pii/S0022024802020560>.
- [31] C. Lan, B. Yeh, Three-dimensional simulation of heat flow, segregation, and zone shape in floating-zone silicon growth under axial and transversal magnetic fields, *J. Cryst. Growth* 262 (1) (2004) 59–71, <https://doi.org/10.1016/j.jcrysgr.2003.09.055>. URL: <http://www.sciencedirect.com/science/article/pii/S0022024803019080>.
- [32] G. Ratnicks, A. Muiznieks, A. Mühlbauer, Modelling of phase boundaries for large industrial FZ silicon crystal growth with the needle-eye technique, *J. Cryst. Growth* 255 (3) (2003) 227–240, [https://doi.org/10.1016/S0022-0248\(03\)01253-3](https://doi.org/10.1016/S0022-0248(03)01253-3). URL: <https://www.sciencedirect.com/science/article/pii/S0022024803012533>.
- [33] A. Mühlbauer, A. Muiznieks, J. Virbulis, A. Lüdge, H. Riemann, Interface shape, heat transfer and fluid flow in the floating zone growth of large silicon crystals with the needle-eye technique, *J. Cryst. Growth* 151 (1) (1995) 66–79, [https://doi.org/10.1016/0022-0248\(95\)00027-5](https://doi.org/10.1016/0022-0248(95)00027-5). URL: <https://www.sciencedirect.com/science/article/pii/0022024895000275>.
- [34] A. Sabanskis, K. Sururov, J. Virbulis, 3d modeling of doping from the atmosphere in floating zone silicon crystal growth, *J. Cryst. Growth* 457 (2017) 65–71, <https://doi.org/10.1016/j.jcrysgr.2016.10.048>. URL: <https://www.sciencedirect.com/science/article/pii/S0022024816301865>.
- [35] X.F. Han, X. Liu, S. Nakano, H. Harada, Y. Miyamura, K. Kakimoto, 3D Global Heat Transfer Model on Floating Zone for Silicon Single Crystal Growth, *Cryst. Res. Technol.* 53 (5) (2018) 1–5, <https://doi.org/10.1002/crat.20170246>.
- [36] X.F. Han, X. Liu, S. Nakano, H. Harada, Y. Miyamura, K. Kakimoto, 3D numerical simulation of free surface shape during the crystal growth of floating zone (FZ) silicon, *J. Cryst. Growth* 483 (2018) 269–274, <https://doi.org/10.1016/j.jcrysgr.2017.12.012>.
- [37] J. Fan, R. Liang, Effects of thermocapillary convection and shear flow on the distribution of inclusions in half-floating zones, *J. Cryst. Growth* 587 (2022) 126639, <https://doi.org/10.1016/j.jcrysgr.2022.126639>. URL: <https://www.sciencedirect.com/science/article/pii/S0022024822001270>.
- [38] H.M. Ettouney, R.A. Brown, Finite-element methods for steady solidification problems, *J. Comp. Phys.* 49 (1983) 118–150.
- [39] A. Yeckel, J.J. Derby, Computational simulations of the growth of crystals from liquids, in: H. Scheel, T. Fukuda (Eds.), *Crystal Growth Technology*, John Wiley & Sons, West Sussex, UK, 2003, pp. 115–137 (Chapter 6).
- [40] J.J. Derby, A. Yeckel, Heat transfer analysis and design for bulk crystal growth: Perspectives on the Bridgman method, in: T. Nishinaga, P. Rudolph (Eds.), *Handbook of Crystal Growth*, Part A, second ed., vol. II, Elsevier, 2015, pp. 793–843 (Chapter 20).
- [41] K.A. Jackson, Mechanism of growth, in: *Liquid Metals and Solidification*, Am. Soc. Metals, 1958, pp. 174–186.
- [42] T. Surek, B. Chalmers, The direction of growth of the surface of a crystal in contact with its melt, *J. Cryst. Growth* 29 (1975) 1.
- [43] T. Surek, S.R. Coriell, B. Chalmers, The growth of shaped crystals from the melt, *J. Cryst. Growth* 50 (1980) 21–32.
- [44] A. Virozub, I.G. Rasin, S. Brandon, Revisiting the constant growth angle: Estimation and verification via rigorous thermal modeling, *J. Cryst. Growth* 310 (24) (2008) 5416–5422.
- [45] N. Eustathopoulos, B. Drevet, S. Brandon, A. Virozub, Basic Principles of Capillarity in Relation to Crystal Growth, in: T. Duffar (Ed.), *Crystal Growth Processes Based on Capillarity: Czochralski, Floating Zone, Shaping and Crucible Techniques*, John Wiley & Sons Ltd, 2010, pp. 1–49. <https://doi.org/10.1002/9781444320237.ch1> (Chapter 1).
- [46] G. Strang, G.J. Fix, *An Analysis of the Finite Element Method*, Prentice-Hall, Inc., Englewood Cliffs, NJ, 1973.
- [47] G. Dhatt, G. Touzot, *The Finite Element Method Displayed*, John Wiley and Sons, New York, 1984.
- [48] P. Gresho, R. Sani, *Incompressible Flow and the Finite Element Method: Advection-Diffusion and Isothermal Laminar Flow*, first ed., John Wiley and Sons, New York, 1998.
- [49] T.J.R. Hughes, *The Finite Element Method: Linear Static and Dynamic Finite Element Analysis*, Dover Publications, Inc., Mineola, New York, 2000.

- [50] R.A. Cairncross, P.R. Schunk, T.A. Baer, R.R. Rao, P.A. Sackinger, A finite element method for free surface flows of incompressible fluids in three dimensions. Part I. Boundary fitted mesh motion, *Int. J. Numer. Meth. Fluids* 33 (3) (2000) 375–403.
- [51] P.A. Sackinger, P.R. Schunk, R.R. Rao, A Newton-Raphson pseudo-solid domain mapping technique for free and moving boundary problems: A finite element implementation, *J. Comput. Phys.* 125 (1) (1996) 83–103, <https://doi.org/10.1006/jcph.1996.0081>.
- [52] X.S. Li, An overview of SuperLU: Algorithms, implementation, and user interface, *ACM Trans. Math. Softw.* 31 (3) (2005) 302–325.
- [53] P.R. Schunk, GOMA 6.0: A full-Newton finite element program for free and moving boundary problems with coupled fluid/solid momentum, energy, mass, and chemical species transport: User's guide, Tech. Rep. SAND2013-1844, Sandia National Laboratories, 2013.
- [54] H.B. Keller, Numerical solution of bifurcation and nonlinear eigenvalue problems, in: P.H. Rabinowitz (Ed.), *Applications of Bifurcation Theory*, Academic Press, New York, 1977, pp. 359–384.
- [55] D. Rivas, J. Sanz, C. Vázquez, Temperature field in a cylindrical crystal heated in a mono-ellipsoid mirror furnace, *J. Cryst. Growth* 116 (1) (1992) 127–138, [https://doi.org/10.1016/0022-0248\(92\)90122-Y](https://doi.org/10.1016/0022-0248(92)90122-Y). URL: <http://www.sciencedirect.com/science/article/pii/002202489290122Y>.
- [56] D. Rivas, R. Haya, A conduction–radiation model for the floating-zone technique in monoellipsoidal mirror furnaces, *J. Cryst. Growth* 206 (3) (1999) 230–240, [https://doi.org/10.1016/S0022-0248\(99\)00340-1](https://doi.org/10.1016/S0022-0248(99)00340-1). URL: <http://www.sciencedirect.com/science/article/pii/S0022024899003401>.
- [57] D. Rivas, C. Vázquez-Espi, An analysis of lamp irradiation in ellipsoidal mirror furnaces, *J. Cryst. Growth* 223 (3) (2001) 433–445, [https://doi.org/10.1016/S0022-0248\(01\)00676-5](https://doi.org/10.1016/S0022-0248(01)00676-5). URL: <http://www.sciencedirect.com/science/article/pii/S0022024801006765>.
- [58] D. Rivas, R. Haya, Analysis of secondary radiation (multiple reflections) in monoellipsoidal mirror furnaces, *J. Cryst. Growth* 241 (1) (2002) 249–260, [https://doi.org/10.1016/S0022-0248\(02\)01259-9](https://doi.org/10.1016/S0022-0248(02)01259-9). URL: <http://www.sciencedirect.com/science/article/pii/S0022024802012599>.
- [59] D. Rivas, Simulation of microgravity floating-zone crystal-growth experiments in monoellipsoidal mirror furnaces, *J. Cryst. Growth* 262 (1) (2004) 48–58, <https://doi.org/10.1016/j.jcrysGro.2003.09.051>. URL: <http://www.sciencedirect.com/science/article/pii/S0022024803019079>.
- [60] D. Souptel, W. Löser, G. Behr, Vertical optical floating zone furnace: Principles of irradiation profile formation, *J. Crystal Growth. Sci.* 300 (2007) 538–550.
- [61] G. Behr, W. Löser, N. Wizent, P. Ribeiro, M.-O. Apostu, D. Souptel, Influence of heat distribution and zone shape in the floating zone growth of selected oxide compounds, *J. Mater. Sci.* 45 (2010) 2223–2227.
- [62] P.J. Hart, Distribution of Radiation From Elliptical and Parabolic Mirrors, *J. Opt. Soc. Am.* 48 (9) (1958) 637–642. URL: <http://www.ncbi.nlm.nih.gov/pubmed/18822346>.
- [63] D. Souptel, W. Löser, G. Behr, Vertical optical floating zone furnace: Principles of irradiation profile formation, *J. Cryst. Growth* 300 (2) (2007) 538–550, <https://doi.org/10.1016/j.jcrysGro.2006.12.042>.
- [64] N. Zhang, H.G. Park, J.J. Derby, Simulation of heat transfer and convection during sapphire crystal growth in a modified heat exchanger method, *J. Cryst. Growth* 367 (2013) 27–34, <https://doi.org/10.1016/j.jcrysGro.2013.01.011>.
- [65] S.S. Dossa, Modeling the high-pressure optical floating zone crystal growth system and the high-pressure, high-temperature growth of single-crystal diamond, Ph.D. thesis, University of Minnesota (in preparation 2022).
- [66] P.M. Gresho, Modification of the FEM3 model to ensure mass conservation, Tech. rep., Lawrence Livermore National Laboratory (1987).
- [67] B. Younglove, Thermophysical Properties of Fluids. 1. Argon, Ethylene, Parahydrogen, Nitrogen, Trifluoride, and Oxygen, in: NIST Chemistry WebBook, NIST Standard Reference Database 69, 20899th Edition, National Institute of Standards and Technology, Gaithersburg MD, 2021, Ch. Thermophys. doi:<https://doi.org/10.18434/T4D303>.
- [68] A.E. Gill, The boundary-layer regime for convection in a rectangular cavity, *J. Fluid Mech.* 26 (3) (1966) 515–536, <https://doi.org/10.1017/S0022112066001368>.
- [69] J.J. Derby, Fluid dynamics in crystal growth: The good, the bad, and the ugly, *Prog. Cryst. Growth Charact. Mater.* 62 (2016) 286–301.
- [70] R. Siegel, J.R. Howell, *Thermal Radiation Heat Transfer*, Third Edition, McGraw-Hill, New York, 1993.
- [71] S. Kuppurao, J.J. Derby, Finite element formulations for accurate calculation of radiant heat transfer in diffuse-gray enclosures, *Numer. Heat Transf. Part B: Fundam.* 24 (431–454) (1993).
- [72] S. Brandon, J.J. Derby, Internal radiative transport in the vertical Bridgman growth of semitransparent crystals, *J. Cryst. Growth* 110 (1991) 481–500.
- [73] S. Brandon, J.J. Derby, Heat transfer in vertical Bridgman growth of oxides: Effects of conduction, convection, and internal radiation, *J. Cryst. Growth* 121 (1992) 473–494.
- [74] S. Brandon, J.J. Derby, A finite element method for conduction, internal radiation, and solidification in a finite axisymmetric enclosure, *Int. J. Num. Meth. Heat Fluid Flow* 2 (1992) 299–333.
- [75] G. Samanta, A. Yeckel, P. Daggolu, H. Fang, E.D. Bourret-Courchesne, J.J. Derby, Analysis of limits for sapphire growth in a micro-pulling-down system, *J. Cryst. Growth* 335 (1) (2011) 148–159, <https://doi.org/10.1016/j.jcrysGro.2011.09.015>. URL: <http://www.sciencedirect.com/science/article/pii/S0022024811007585>.
- [76] G. Samanta, A. Yeckel, E.D. Bourret-Courchesne, J.J. Derby, Parametric sensitivity and temporal dynamics of sapphire crystal growth via the micro-pulling-down method, *J. Cryst. Growth* 359 (2012) 99–106, <https://doi.org/10.1016/j.jcrysGro.2012.08.037>. URL: <http://www.sciencedirect.com/science/article/pii/S0022024812006008>.
- [77] Committee for an Assessment of and Outlook for New Materials Synthesis and Crystal Growth, *Frontiers in Crystalline Matter: From Discovery to Technology*, no. ISBN: 0-309-13801-9, National Research Council, 2009.